

# Sub-Parts Per Million NO<sub>2</sub> Chemi-Transistor Sensors Based on Composite Porous Silicon/Gold Nanostructures Prepared by Metal-Assisted Etching

Michela Sainato,<sup>†</sup> Lucanos Marsilio Strambini,<sup>†</sup> Simona Rella,<sup>‡</sup> Elisabetta Mazzotta,<sup>‡</sup> and Giuseppe Barillaro<sup>\*,†</sup>

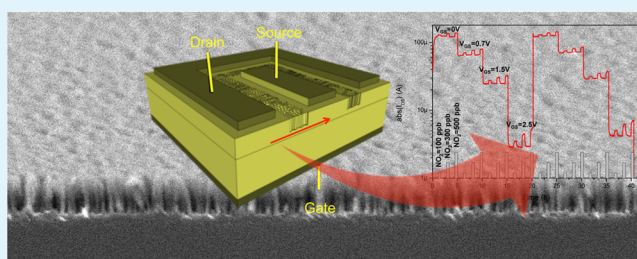
<sup>†</sup>Dipartimento di Ingegneria dell'Informazione, Università di Pisa, Via G. Caruso 16, 56122 Pisa, Italy

<sup>‡</sup>Dipartimento di Scienze e Tecnologie Biologiche e Ambientali, Università del Salento, Via Monteroni, 73100 Lecce, Italy

## S Supporting Information

**ABSTRACT:** Surface doping of nano/mesostructured materials with metal nanoparticles to promote and optimize chemi-transistor sensing performance represents the most advanced research trend in the field of solid-state chemical sensing. In spite of the promising results emerging from metal-doping of a number of nanostructured semiconductors, its applicability to silicon-based chemi-transistor sensors has been hindered so far by the difficulties in integrating the composite metal–silicon nanostructures using the complementary metal-oxide-semiconductor (CMOS) technology. Here we propose a facile and effective top-down method for the high-yield fabrication of chemi-transistor sensors making use of composite porous silicon/gold nanostructures (cSiAuNs) acting as sensing gate. In particular, we investigate the integration of cSiAuNs synthesized by metal-assisted etching (MAE), using gold nanoparticles (NPs) as catalyst, in solid-state junction-field-effect transistors (JFETs), aimed at the detection of NO<sub>2</sub> down to 100 parts per billion (ppb). The chemi-transistor sensors, namely cSiAuJFETs, are CMOS compatible, operate at room temperature, and are reliable, sensitive, and fully recoverable for the detection of NO<sub>2</sub> at concentrations between 100 and 500 ppb, up to 48 h of continuous operation.

**KEYWORDS:** porous silicon, metal nanostructure, composite nanomaterial, chemi-transistor, gas sensing, nitrogen dioxide



## 1. INTRODUCTION

Detection of NO<sub>2</sub> has become increasingly marked for environmental control and personal safety because of its dangerous effects on human health and environment, and its large emission from on-road vehicle and industrial process exhaust, as reported by the European Environment Agency (EEA).<sup>1</sup> This fact leads to stringent regulatory laws and controls on exhaust emissions level and composition and, in turn, to the need for miniaturized sensors with low limit of detection, high sensitivity, high throughput, with small cross-sensitivity, for a reliable detection of NO<sub>2</sub> at concentration as low as 53 ppb.<sup>2</sup>

Commercial NO<sub>2</sub> sensors are typically chemi-resistive and make use of semiconducting metal oxides, such as tin oxide (SnO<sub>2</sub>), tungsten oxide (WO<sub>3</sub>), or zinc oxide (ZnO). Although they do show excellent sensitivity, limit of detection is typically 1 ppm and operation temperature is in the range of 200–600 °C.<sup>3</sup> Challenges are reduction of power consumption because of the high operation temperature, as well as improvement of the limit of detection.

Because of their amplified response, lower-temperature operation, and tunable sensitivity, with respect to chemi-resistor sensors, chemi-transistor sensors<sup>4,5</sup> have led to extensive research and their impact can be easily envisaged

from analysis of markets related to healthcare, environmental control, and food safety.

Moreover, chemi-transistor sensors based on nano/mesostructured materials have demonstrated to outperform their standard counterpart making use of bulk materials. This is due to the higher surface area and higher chemical affinity of materials at the nano/mesoscale that allow a more effective interaction with molecules coming from the surrounding environment. Examples are carbon nanotubes,<sup>6</sup> graphene,<sup>7</sup> porous silicon (PS),<sup>8</sup> metal-oxide nanowires,<sup>9</sup> organic polymers,<sup>10</sup> and silicon nanowires.<sup>11,12</sup>

Remarkably, surface doping of these nano/mesostructured materials to promote and optimize the chemi-transistor sensing characteristics represents a significant advance in the field of solid-state chemical sensing. Excellent works concerning the modification of flat<sup>13</sup> and nano/mesostructured semiconductors via surface decoration with both metal and metal-oxide nanoclusters/particles with size- and shape-dependent physicochemical properties have been reported for metal oxides,<sup>14</sup> carbon nanotubes,<sup>15</sup> and III–V semiconductors.<sup>16</sup> Commonly

**Received:** December 19, 2014

**Accepted:** March 16, 2015

**Published:** March 16, 2015

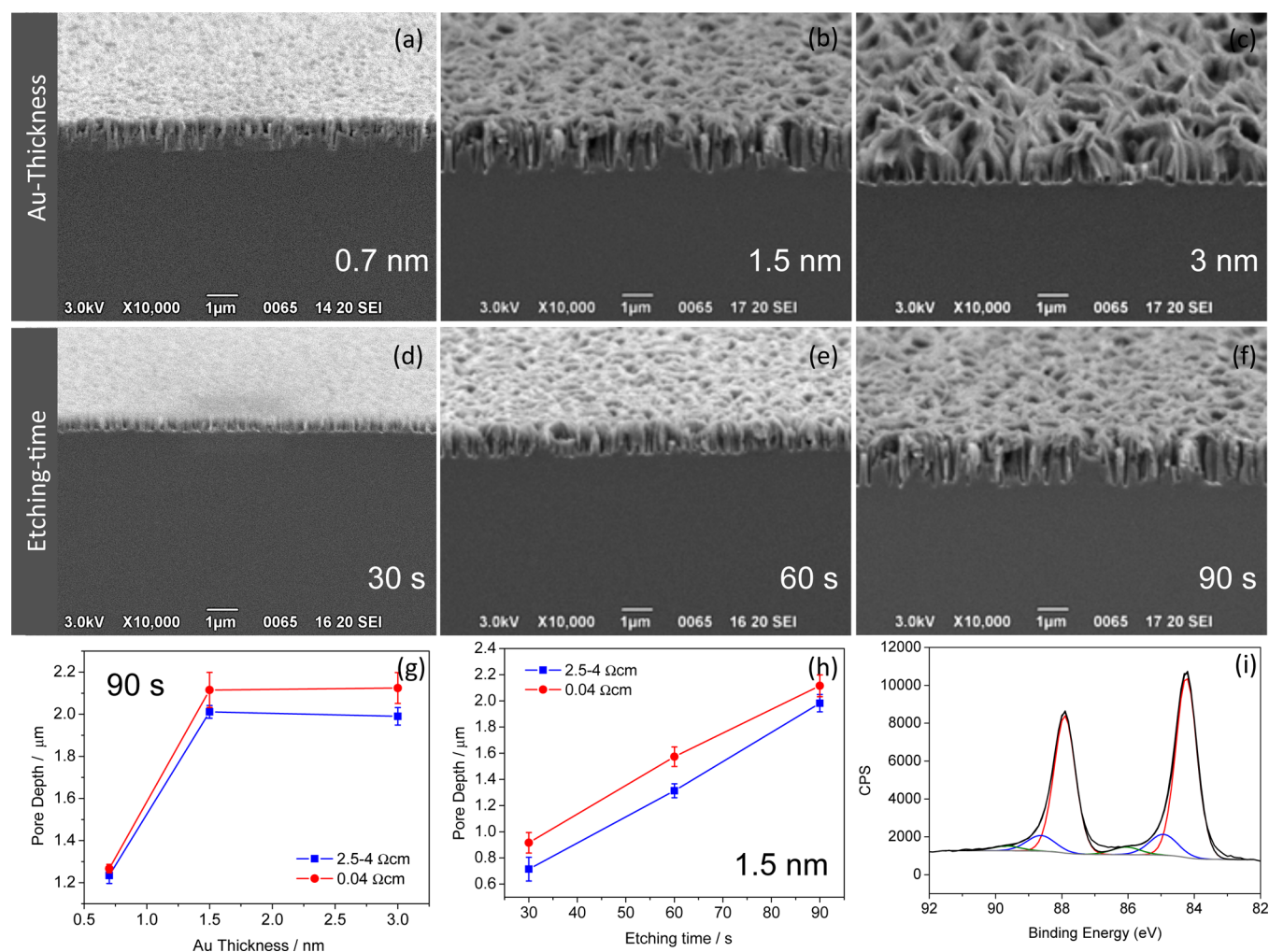


**Figure 1.** Preparation and characterization of composite porous silicon/gold nanostructures (cSiAuNs) obtained by gold-assisted etching on (100) p-type Si in HF/H<sub>2</sub>O<sub>2</sub> solution. (a–f) Cross-sectional scanning electron microscopy (SEM) images of cSiAuNs obtained: with fixed etching time of 90 s and different nominal gold thicknesses of (a) 0.7, (b) 1.5, and (c) 3 nm; with fixed nominal gold thickness of 1.5 nm and different etching times of (d) 30, (e) 60, and (f) 90 s. (g, h) cSiAuN pore depth as a function of (g) Au thickness and (h) etching time. (i) X-ray photoelectron spectroscopy (XPS) analysis highlighting Au 4f resolved spectra on cSiAuNs.

exploited dopants for the detection of NO<sub>2</sub> and nitrogen oxide (NO), namely NO<sub>x</sub>, include noble metals such as Pb, Pt, Ag, and Au nanoparticles (NPs), because of their privileged catalytic properties and distinctive selectivity toward NO<sub>x</sub> gases.<sup>14,16,15,17,18</sup> The inclusion of metal nanoparticles on the nanostructured semiconductors leads to the synthesis of composite metal–semiconductor materials with enhanced sensing capabilities achieved by bringing the catalytic properties of the metal nanoparticles and the widely tunable bandgap of the nanostructured semiconductors into play. In such composite materials, metal nanostructures act as gateways able to influence the transit of electrons to and from the semiconductor interface onto which they are deposited. This gives rise to large and fast changes in the electrical properties of the sensing material upon interaction with specific analytes, which translate into an improvement of the chemi-transistor response in terms of dynamics, sensitivity, and more important, selectivity.

In spite of the promising results emerging from metal-doping of a number of nanostructured semiconductors, its applicability to silicon-based chemi-transistor sensors has been hindered by the difficulties in integrating the composite metal–silicon

nanostructures using the complementary metal-oxide-semiconductor (CMOS) technology. Silicon-based chemi-transistors have various advantages over the other nanomaterial-based ones, because the former can exploit well-developed CMOS technology and process to integrate the chemi-transistors into small chips together with control and readout electronics, thus envisaging fabrication of sensing chips at low cost. As to metal-doped silicon chemi-transistors, only recently a silicon-nanowire chemi-transistor decorated with Pd nanoparticles has been reported for H<sub>2</sub> sensing.<sup>19</sup>

Here we propose a facile and effective top-down method for the high-yield fabrication of chemi-transistor sensors making use of composite porous silicon/gold nanostructures (cSiAuNs) acting as sensing gate. In particular, we investigate the integration of cSiAuNs synthesized by metal-assisted etching (MAE),<sup>20,21</sup> using gold NPs as catalyst, in solid-state junction-field-effect transistors (JFETs), aimed at the detection of NO<sub>2</sub> down to 100 parts per billion (ppb). The chemi-transistor sensors, namely cSiAuJFETs, operate at room temperature and are reliable, sensitive, and fully recoverable for the detection of NO<sub>2</sub> at concentrations between 100 and 500 ppb, up to 48 h of continuous operation. We argue that

adsorption of NO<sub>2</sub> on the cSiAuN surface modifies the fixed charge of cSiAuNs by efficiently depleting of free electrons the silicon nanostructure via gold nanoparticle mediation and, in turn, by modulating the width of the space-charge region at the cSiAuN/JFET-channel interface. This accounts for the fast and reliable variation of the sensor current at such low NO<sub>2</sub> concentrations. Moreover, the possibility of tuning the thickness and to control the morphology of the composite porous silicon/gold nanostructures is also investigated, thus envisaging versatile physical and chemical properties of this material as sensing gate toward the detection of NO<sub>2</sub>.

To the best of our knowledge, the use of MAE for the integration of nanostructured silicon/metal composites into chemi-transistor sensors has not been reported so far and represents a great potential for the fabrication of metal-doped (e.g., using Au, Ag, Pt) silicon-based chemi-transistors with peculiar sensing features, in terms of sensitivity and selectivity, toward specific gases. In fact, although significant efforts have been devoted to energy conversion application of silicon nanostructures prepared by MAE,<sup>22,23</sup> only one work on their gas sensing property has been reported using a chemi-resistor sensor.<sup>24</sup>

## 2. SYNTHESIS AND CHARACTERIZATION OF COMPOSITE POROUS SILICON/GOLD NANOSTRUCTURES

Synthesis of composite porous silicon/gold nanostructures using MAE is thoroughly investigated by chemical etching of silicon in HF/H<sub>2</sub>O<sub>2</sub> solution activated by gold nanoparticles deposited on the Si surface by electron-beam assisted thermal evaporation, as given in the literature.<sup>25–27</sup> A systematic study is carried out on p and p<sup>+</sup> silicon so as to investigate influence of nominal gold-thickness and etching-time on both morphology and pore depth of the resulting cSiAuNs versus silicon resistivity.

It is well-known that by properly tuning thermal evaporation parameters, e.g. temperature, partial pressure, thickness and deposition rate, for nominal thickness in the nanometer range the metal film coating gives rise to a surface coverage not fully connected and forms metal nanoparticles or nanoislands that have similar distribution density and size, thus leaving sections of the silicon surface free from metal.<sup>28–30</sup> With all the other parameters fixed, the features of metal NPs are deeply dependent on the nominal thickness of the film deposited, which, in turn, is deeply affecting the resulting etched silicon nanostructure. Size, shape, and distribution of the gold NPs change as the nominal thickness of the evaporated gold film increases, from a few isolated nanoparticles of spherical shape with uniform distribution, to partially interconnected patches of elongated NPs that tend to coalesce and form clusters.<sup>31</sup>

According to the commonly accepted mechanism for MAE of silicon,<sup>25,27</sup> after immersion of the samples in solution of HF and H<sub>2</sub>O<sub>2</sub>, gold NPs rapidly sink into the Si bulk following the main crystallographic direction (100) of the silicon substrate, thus creating, as a result, pores in the Si substrate or, additionally, Si wires. The reaction mechanism consists in the reduction of H<sub>2</sub>O<sub>2</sub>, promoted by metal clusters, and the oxidation of Si, subsequently etched by F<sup>−</sup> ions. Because of the catalytic activity of metal, holes (h<sup>+</sup>) from the reduction of the oxidative agent are injected into the valence band of silicon, therefore causing the Si etching right underneath the metal clusters because of the much faster etching of the Si under metal catalyst than Si without metal coverage.<sup>32,33</sup>

Figure 1a–c shows scanning electron microscope (SEM) images of different cSiAuNs obtained from silicon samples coated with different nominal gold-thickness films, namely 0.7, 1.5, and 3 nm, and etched for a fixed time of 90 s.

First, we observe that morphology of pores and diameter of pillars of the cSiAuNs resulting from the MAE process significantly depend on the nominal thickness of the metal film deposited on top of the silicon surface and, in turn, on the size and distribution of the Au NPs evaporated. In our experiments, 0.7 nm thick Au coating on the silicon surface corresponds to a low distribution density of the metal NPs, which leads to low porosity cSiAuNs with vertical pores separated by crystalline silicon pillars with size comparable to the pore diameter (Figure 1a). Lift-off or Brownian movement of the metal NPs may occur during the silicon dissolution in the case of thin film thickness, therefore contributing to the formation of noncolumnar silicon nanostructures.<sup>34,35</sup> On the other hand, thicker metal films of 1.5 nm lead to higher NP density and, consequently, to higher porosity cSiAuNs with columnar morphology, where pores are separated by thin silicon pillars with more uniform cross-sectional shape and height (Figure 1b). According to the literature,<sup>36</sup> by further increasing the metal thickness up to 3 nm and, in turn, the density of NPs, both porosity and aspect ratio of the resulting cSiAuNs are increased, up to the formation of silicon nanowires (SiNWs). In fact, deposition of thicker gold layer through thermal evaporation leads to the formation of nonuniform NPs with higher distribution density that tend to coalesce and form clusters.<sup>31</sup> The resulting etched nanostructures consist on thin walls of Si (the nanowires) that tend to collapse in triangular shape inclined of 38° (Figure 1c).<sup>31</sup> A clustering at the silicon wire tips due to critical forces acting at the meniscus between air and pentane during the final drying step is observed.<sup>29</sup>

Further characterization is performed on cSiAuNs obtained from the 1.5 nm thick Au coating (Figure 1b) because of both its larger specific surface area compared to the composite nanostructures obtained from 0.7 nm thick Au coating (Figure 1a), and its higher fabrication reliability in terms of mechanical stability compared to the composite nanostructures obtained from 3 nm thick Au coating (Figure 1c).

Figure 1d–f shows SEM images of cSiAuNs obtained with 1.5 nm thick Au coating and etched at different times in a range of 30 to 90 s, with a step of 30 s. By tuning the etching time we are able to control the composite porous silicon/gold nanostructure thickness. cSiAuNs maintain the same well-defined homogeneous columnar morphology, whereas the thickness of the layer linearly increases in a range from 680 nm to 2 μm, from 30 to 90 s, because of the further sinking of metal nanoparticles upon prolonged immersion in the HF/H<sub>2</sub>O<sub>2</sub> solution.

The relationship between cSiAuN main parameters, namely pore depth, Au thickness, and etching time is summarized in Figure 1g,h, which reports silicon pore depth as a function of Au-thickness coating (at constant etching time of 90 s) and of etching time (at constant Au thickness of 1.5 nm), respectively. Figure 1g shows that cSiAuN layers exhibit a depth from 1.2 μm to about 2 μm, when Au thickness varies from 0.7 to 3 nm. In particular, the increase in metal layer thickness from 0.7 to 1.5 nm determines a steep increase of nanostructure depth, which reflects an augmented etching rate as the nominal metal thickness changes from 0.7 to 1.5 nm. This augmented etching rate is due to the increasing physical access of the etchant to the area<sup>31</sup> underneath Au nanoislands (active site), which is related



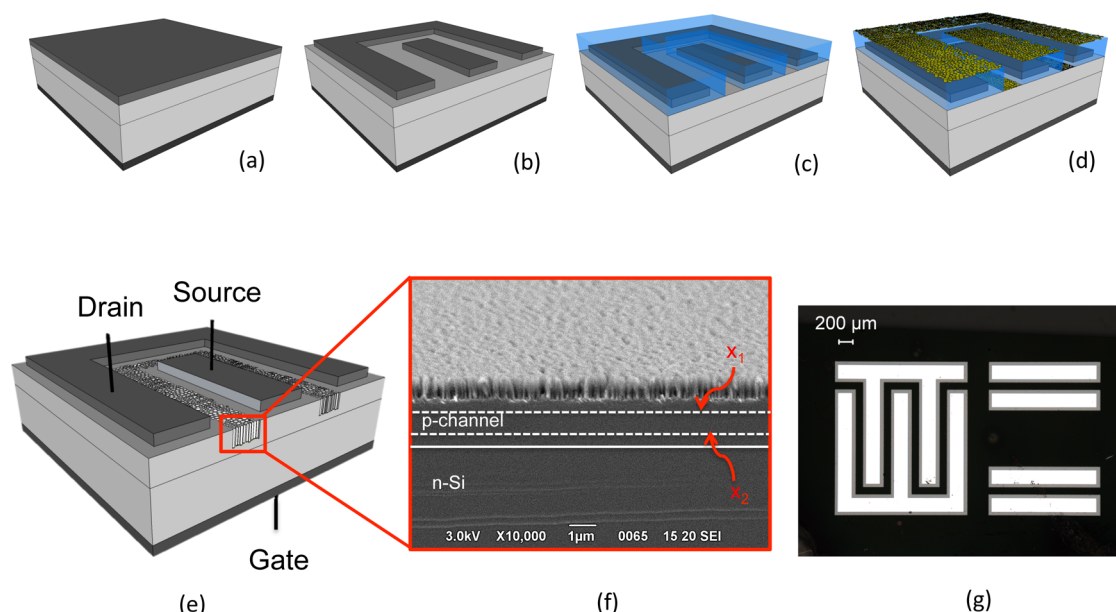


**Figure 2.** Main fabrication steps of the cSiAuJFET sensor: (a) pn silicon wafer (nominal resistivity of p-type layer and n-type substrate of 0.04 and 2–4  $\Omega$  cm, respectively) with 500 nm thick aluminum on both front and back-side surfaces; (b) definition of source (S) and drain (D) terminals of the JFET device by standard photolithography; (c) S and D contact protection by using a patterned photoresist layer; (d) e-beam thermal evaporation of a 1.5 nm thick gold layer to obtain gold nanoparticles covering the p-type silicon surface between S and D contacts; (e) synthesis of cSiAuNs between S and D contacts of the JFET device by Au-assisted etching in HF/H<sub>2</sub>O<sub>2</sub> solution. (f) Scanning electron microscopy (SEM) cross-sectional image of the typical cSiAuN selectively integrated between S and D terminals of the JFET device, with the depletion regions at the cSiAuN/p-channel interface and at the p-channel/n-silicon interface,  $x_1$  and  $x_2$ , respectively, highlighted. (g) Optical microscope top-view of cSiAuJFET sensors with different S/D configurations: comb-type on the left and parallel-plate on the right.

to the increase of grain size and coalescence of gold NPs and, in turn, determined by the augmented thickness of metal film deposited.<sup>21,37</sup> By further increasing Au thickness, cSiAuN depth becomes slightly dependent on both size and distribution of metal NPs and the depth-thickness curve tends to saturate around 2  $\mu$ m of pore depth (Figure 1g). Such a behavior can be explained by considering that the catalytic activity of Au nanoparticles has been demonstrated to be very sensitive to the ratio between Au particle size and Au/semiconductor perimeter interface.<sup>38,39</sup> For clusters in an intermediate size range (Au thickness between 1.5 and 3 nm), defect energies from the edge and corner atoms become non-negligible and the ratio between the size of clusters and the perimeter interface is similar, thus leading to the same physical access area to the etchant. Moreover, Figure 1g also points out that the catalytic activity of gold NPs is not critically influenced by the doping of silicon on which they are deposited, leading to similar etching rate Au-covered (under identical conditions) regions both on a p<sup>+</sup> (0.04  $\Omega$  cm) (Figure 1g, red line) and on a p (2.5–4  $\Omega$  cm) (Figure 1g, blue line) Si substrates that differ from 2 orders of magnitude in resistivity.<sup>40</sup>

Concerning the relationship between etching rate and doping level, for Au-covered (under identical conditions) regions on p<sup>+</sup> (0.04  $\Omega$  cm) and on p (2.5–4  $\Omega$  cm) Si substrates (Figure 1h, red line and blue line, respectively), only small variations in pore size and etching depth are observed, according to literature.<sup>41</sup> With all the other parameters fixed, the Au-coated area on the highly doped p<sup>+</sup> Si is etched into a columnar porous structure with slightly deeper pores (between 200 and 300 nm higher) but same rate of dissolution (20 nm/s), with respect to the one obtained with low doped p Si (Figure 1h, blue line).<sup>40</sup>

The presence of gold NPs on the porous silicon matrix is verified by X-ray photoelectron spectroscopy (XPS) analysis of cSiAuNs, also providing information about both composition and oxidation states of the deposited metal NPs and of the nanostructured silicon surface.

As shown in Figure 1i, the Au 4f core level spectrum in cSiAuN exhibits a principal component with 4f<sub>5/2</sub> and 4f<sub>7/2</sub> levels at 87.9 and 84.2 eV, respectively. It is interesting to observe the small shift of 0.3 eV in the core-level binding energy in respect to Au foil (for which 4f<sub>5/2</sub> and 4f<sub>7/2</sub> peaks are located at 87.6 and 83.9 eV, respectively) that could be ascribed to quantum size effect of NPs.<sup>42</sup> Two other components located at higher binding energy (one at 88.6 and 85.0 eV and a less intense one at 89.6 and 86.0 eV) can be identified. These features can be attributed to gold silicide (Au<sub>x</sub>Si), in good agreement with literature data<sup>42–44</sup> reporting the formation of intermetallic species Au<sub>x</sub>Si with  $x$  going from 2 to 7<sup>45</sup> during AuNP deposition on silicon, composed of Au at different oxidation states that originates several components in the Au 4f spectrum at higher binding energies than that of metallic Au. The experimental ratio between peak areas of the metallic Au and Au<sub>x</sub>Si components is estimated to be equal to 5. The presence of Au<sub>x</sub>Si species is further confirmed by the analysis of Si 2p signal (data not shown) exhibiting three different components, specifically at 100.0 eV attributable to Si–Si bonds, at 102.4 eV due to the contribution of Si 2p states in gold silicide, and at 103.7 eV attributable to SiO<sub>2</sub>.<sup>44</sup>

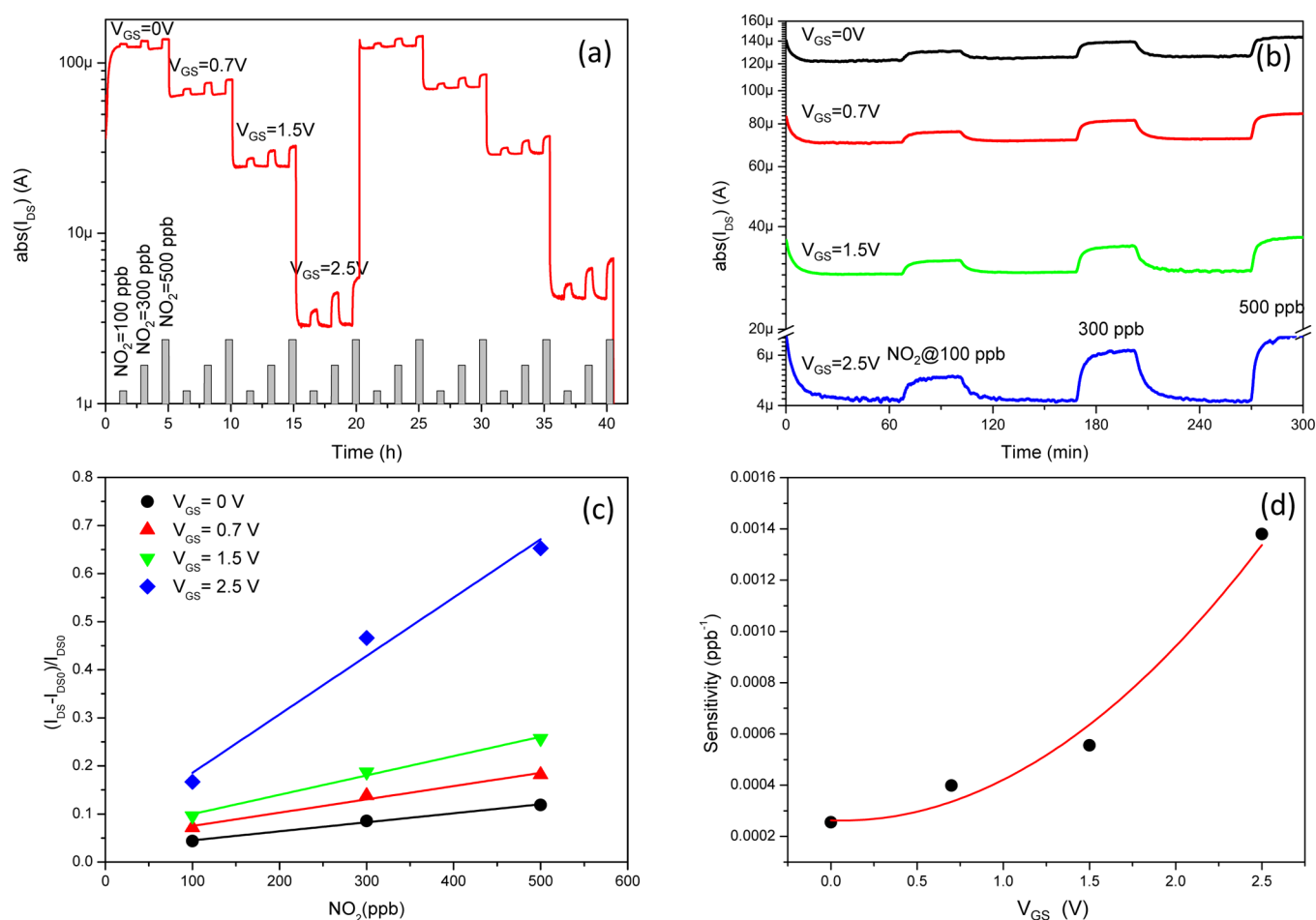


**Figure 3.** Characterization and performance of parallel-plate cSiAuJFET sensor: (a) Time-resolved curve (current versus time) of cSiAuJFET measured upon  $\text{NO}_2$  exposure at concentration of 100, 300, 500 ppb for different polarization voltages  $V_{\text{GS}}$  (from 0 to 2.5 V) up to 48 h of continuous operation and (b) in a narrower time-window (5 h). (c) Relative current-variation  $\Delta I_{\text{R}}$  as a function of  $\text{NO}_2$  concentration (calibration curve). (d) Experimental sensitivity curve (sensitivity versus gate voltage  $V_{\text{GS}}$ ) and best-fitting of experimental data with a quadratic curve.

### 3. INTEGRATION OF COMPOSITE POROUS SILICON/GOLD NANOSTRUCTURES INTO A CHEMI-TRANSISTOR PLATFORM

On the basis of the results obtained on the preparation of composite porous silicon/gold nanostructures using different MAE parameters (section 2), cSiAuNs prepared from 1.5 nm thick Au coating and 90 s etching time are selected for the fabrication of chemi-transistor devices, because of both the larger specific surface area and enhanced fabrication reliability.

Through a postprocess step based on MAE of the CMOS compatible process-flow, junction-field-effect transistor (JFET) exploiting a cSiAuN layer as extra sensing-gate is fabricated. The resulting chemi-transistor sensor, namely cSiAuJFET, specifically consists of a p-channel JFET in which the cSiAuN layer is selectively integrated on top of the p-channel between source (S) and drain (D) terminals.

Figure 2 shows a schematic representation of the main process steps required for the integration of the cSiAuN into a JFET device. The cSiAuJFET is fabricated on pn-type silicon wafers (nominal resistivity of p-type and n-type silicon layers of 0.04 and 2–4  $\Omega$  cm, respectively). The metallurgical junction between p- and n-type silicon is located at 2.3  $\mu\text{m}$  from top. The cSiAuJFET sensor is fabricated by defining aluminum source and drain contacts (both comb-like and parallel-plate in shape) on the silicon substrate. Aluminum deposition is

performed both on p-type silicon (front-side surface) and on n-type silicon (back-side surface) (Figure 2a). Both comb-like and parallel-plate source (S) and drain (D) terminals are defined by patterning (1st mask) the aluminum film on top of the p-type silicon (front-side surface) (Figure 2b). Source and drain terminals are then protected using a patterned photoresist layer (2nd mask) (Figure 2c), through which deposition of 1.5 nm thick gold layer on the p-type silicon between source and drain is performed (Figure 2d). Selective gold-assisted chemical etching of part of the p-type silicon between drain and source terminals is performed to produce the composite porous silicon/gold nanostructured layer on top of the p-channel, then the patterned photoresist is removed (Figure 2e). Figure 2e shows the final structure of the chemi-transistor sensor of this work, which is characterized by two independent gates: a solid electrical gate on the back side, which allows the current of the JFET device to be electrically tuned, and a nanostructured sensing gate on the front side, which allows the JFET device to be provided with sensing capability. Figure 2f shows an SEM cross-section of the typical composite porous silicon/gold nanostructured layer that is integrated between drain/source terminals of the JFET and exploited for sensing purposes.

An overall number of 24 cSiAuJFET sensors with same nominal thickness (1.2  $\mu\text{m}$ ) and morphology (columnar-like) of the cSiAuN layer are integrated on the same silicon die over

an area of 1 cm<sup>2</sup>. The sensors feature same channel length  $L = 100\ \mu\text{m}$ , but different drain/source terminals configuration (parallel-plate and comb-type) and size (effective channel widths  $W$  of 300 and 1500  $\mu\text{m}$  for parallel-plate configuration, 3000 and 7500  $\mu\text{m}$  for comb-type configuration). Figure 2g shows an optical microscope top-image of different sensor structures with parallel-plate ( $W = 1500\ \mu\text{m}$ ) and comb-like ( $W = 7500\ \mu\text{m}$ ) drain and source terminals. The cSiAuN (black areas) is clearly visible between source and drain contacts (white areas). Flat silicon surface (gray areas) not involved into the MAE etching step and defined by the difference of first and second patterning masks is also noticeable.

The MAE approach allows fabricating a unique chemi-transistor sensor in which the composite porous silicon/gold nanostructured material acts as a sensing gate, which operates independently of the electrical gate of the JFET device. According to the literature,<sup>8</sup> the nanostructured sensing gate operates by modulating the depletion region width  $x_1$  at the cSiAuN/p-channel interface (Figure 2f) upon adsorption/desorption of analytes on the composite Si/Au nanostructured material itself, thus effectively modulating the p-channel thickness and, in turn, the current flowing in the p-channel dependently on the gas concentration, for a given gate voltage. On the other hand, the electrical gate operates by modulating the depletion region width  $x_2$  at the p-channel/n-silicon interface (Figure 2f) through electrical tuning of the gate terminal voltage of the JFET, thus effectively changing the p-channel thickness and, in turn, the current flowing in the p-channel independently of the gas concentration.

#### 4. DETECTION OF LOW CONCENTRATIONS OF NO<sub>2</sub> USING CHEMI-TRANSISTORS BASED ON COMPOSITE POROUS SILICON/GOLD NANOSTRUCTURES

For gas sensing performance evaluation, the silicon die integrating cSiAuJFET devices is soldered onto a TO-8 support and placed in a stainless steel chamber. A thorough electrical characterization of the cSiAuJFET sensors is performed in NO<sub>2</sub> in the range 100–500 ppb at room temperature (RT), using the flow-through technique, up to 48 h of continuous operation. For all the experiments, flow-rate is maintained at 200 standard cubic centimeter per minute (sccm), synthetic air is used as carrier gas, relative humidity is set to zero, and temperature is set to  $25 \pm 0.5\ ^\circ\text{C}$ . The cSiAuJFETs are biased in the saturation region ( $V_{\text{DS}} = -2\ \text{V}$ ) and exposed to synthetic air for 60 min. This period is necessary to settle the output response of the sensor to a stable current value (warm up period). We argued that desorption of molecules (mostly water with donorlike behavior) adsorbed on the cSiAuN surface during storage in ambient air occurs in this phase, which leads to a decrease of the positive fixed charge of the cSiAuN material and, in turn, to a reduction of the space-charge width in the p-channel underneath the cSiAuNs and to an increase of the current flowing in the p-channel during the warm up period. Afterward the sensors are exposed to NO<sub>2</sub> for 30 min (adsorbing phase) and then to synthetic air for 60 min (desorbing phase), repeating the protocol on the entire concentration window (100–300–500 ppb), whereas the gate voltage (0, 0.7, 1.5, 2.5 V) is tuned at the end of each adsorbing phase of 500 ppb. Time exposure has been chosen based on the “The National Institute for Occupational Safety and Health” (NIOSH) according to “Immediately Dangerous to Life and

Health” (IDLH) levels, which correspond to concentration of the toxic agent after 30 min exposure.<sup>2,46</sup>

Figure 3 reports experimental data on the gas sensing performance typical of cSiAuJFETs with parallel-plate source and drain terminals and with channel width  $W = 1500\ \mu\text{m}$ . Experimental data on the gas sensing performance typical of cSiAuJFETs with comb-type source/drain terminals and with channel width  $W = 7500\ \mu\text{m}$  are reported in Figure S1 in the Supporting Information. For completeness, experimental data simultaneously measured on four cSiAuJFETs with both parallel-plate and comb-type drain/source terminals and different channel widths (300, 1500, 3000, 7500  $\mu\text{m}$ ) are reported in Figure S2 in the Supporting Information.

Figure 3a shows a typical time-resolved curve (current versus time) of cSiAuJFET measured upon NO<sub>2</sub> exposure at concentration of 100, 300, 500 ppb for different gate polarization voltages  $V_{\text{GS}}$  ( $V_{\text{GS}} = 0, 0.7, 1.5, 2.5\ \text{V}$ ). The drain-to-source current  $I_{\text{DS}}$  of each sensor exposed to NO<sub>2</sub> gas is continuously measured for 2 days (up to 48 h) and plotted against time. The total gate current  $I_{\text{G}}$  flowing through the gate terminals of all the sensors under measure is also continuously monitored as control, in order to rule out possible contribution of the gate current changes to the sensor response under NO<sub>2</sub> exposure. The  $I_{\text{G}}$  maximum value is of several hundreds nA and occurs at the highest gate polarization voltage  $V_{\text{GS}} = 2.5\ \text{V}$ , which allows us to rule out significant contribution of the gate current when the sensor current  $I_{\text{DS}}$  is above 1  $\mu\text{A}$ . For this reason, plots of time-resolved curves are limited to  $I_{\text{DS}}$  current values above the threshold value of 1  $\mu\text{A}$ .

The sensors show a reliable behavior independently of the gate voltage values, with the sensor current  $I_{\text{DS}}$  quickly increasing when NO<sub>2</sub> is injected into the test chamber to reach the saturation value in a few minutes and then quickly decreasing when NO<sub>2</sub> is removed from to restore the quiescent current value ( $I_{\text{DS0}}$ ) in synthetic air without significant drift. The effect is evident by repeating the protocol up to 48 h. For each sensor, current changes increase as the NO<sub>2</sub> concentration increases for all the tested  $V_{\text{GS}}$  values. Notably, the sensor behavior is reliable up to 2 days of continuous operation, independently of the polarization-voltage value  $V_{\text{GS}}$ .

The current increase after the exposure to NO<sub>2</sub> could be explained by considering that NO<sub>2</sub> behaves as electron acceptor. According to the theory, on the one hand, the increase in the concentration of free-charge carriers (holes) in cSiAuNs (doping effect) due to adsorption of NO<sub>2</sub> leads to an increase in the cSiAuN conductivity and, in turn, of the current flowing through it.<sup>47,48</sup> On the other hand, the decrease of the (positive) fixed charge density of cSiAuNs due to NO<sub>2</sub> adsorption and consequent formation of NO<sub>2</sub><sup>−</sup> radicals leads to a reduction of the space-charge width in the p-channel underneath the cSiAuNs and, in turn, to an increase in the current flowing in the p-channel.<sup>49,8</sup> According to the literature,<sup>49,8</sup> although the former mainly accounts for the chemi-transistor current variation at higher  $V_{\text{DS}}$  values, the latter accounts for the current variation at lower  $V_{\text{DS}}$  potential values, which is the case of this work. We argue that the small current flowing through the cSiAuNs of the chemi-transistor sensor might account for the noncomplete saturation of the cSiAuJFET current in steady-state conditions.<sup>50</sup>

Figure 3b highlights time-resolved responses of the cSiAuJFET sensor in Figure 3a, for the different NO<sub>2</sub> concentrations and  $V_{\text{GS}}$  values tested, in a narrower time-window (0 to 5 h). On the one hand, the increase of  $V_{\text{GS}}$



produces a reduction of the quiescent current in synthetic air  $I_{DS0}$  from 120  $\mu\text{A}$  at  $V_{GS} = 0\text{ V}$  to about 4  $\mu\text{A}$  at  $V_{GS} = 2.5\text{ V}$ . On the other hand, the increase of the  $\text{NO}_2$  concentration produces a maximum absolute variation of the sensor current  $I_{DS}$  of 20  $\mu\text{A}$  at  $V_{GS} = 0\text{ V}$  and of 7  $\mu\text{A}$  at  $V_{GS} = 2.5\text{ V}$ , for  $\text{NO}_2$  concentration of 500 ppb. For all the tested sensors, it is evident that by increasing the  $V_{GS}$  value the absolute current variation reduces, whereas the relative current variation of the sensor increases. Rise and fall times are about 5 and 10 min, respectively, and only slightly dependent on the values of  $V_{GS}$ , accordingly to the literature on nanostructured chemi-transistor sensors based on JFET devices<sup>8</sup> and differently from those based on MOSFET devices.<sup>51,52</sup> No significant variations in rise and fall times are observed up to 48 h of continuous operation.

Figure 3c reports the relative current variation  $\Delta I_R$  of the sensor in Figure 3a,b as a function of the  $\text{NO}_2$  concentration (calibration curve).  $\Delta I_R$  is by definition  $(I_{DS} - I_{DS0})/I_{DS0}$  in the saturation region at  $V_{DS} = -2\text{ V}$ , where  $I_{DS0}$  is the quiescent current value in air. For all the tested devices, at fixed  $\text{NO}_2$  concentration,  $\Delta I_R$  nonlinearly increases with the  $V_{GS}$  value in the range 0 to 2.5 V; at fixed  $V_{GS}$  values,  $\Delta I_R$  linearly increases with the  $\text{NO}_2$  concentration in the range 0–500 ppb. Notably, all the sensors feature a linear calibration curve within the range of  $\text{NO}_2$  concentrations investigated.

Calculation of sensitivity ( $S$ ), by definition  $S = \partial\Delta I_R/\partial[\text{NO}_2]$ , is performed by taking the slope of the linear regression curve best-fitting the experimental data of Figure 3c, for each tested  $V_{GS}$  value within the  $\text{NO}_2$  window of concentrations tested. Figure 3d shows the values of sensitivity as a function of the  $V_{GS}$  voltage values typical of sensors with parallel-plate drain/source configuration (please, refer to Figure S1b,c for comb-type configuration). Experimental data in Figure 3d are best-fitted with a quadratic curve, which highlights the nonlinear dependence of the sensitivity on the  $V_{GS}$  voltage, for the case of parallel-plate devices (comb-type devices show a linear dependence of the sensitivity value on the gate voltage). It is worth noting that, for  $V_{GS}$  values between 0 and 2.5 V the sensitivity of the cSiAuJFET in Figure 3 can be varied of a factor of 5.6 from  $2.5 \times 10^{-4}\text{ ppb}^{-1}$  to  $1.4 \times 10^{-3}\text{ ppb}^{-1}$ , thus demonstrating that tuning of this key parameter can be used to adjust the sensor response in real-time without the need of using wide dynamic-range voltages. A variation of the gate voltage from 0 to 0.7 V is adequate to scale the value of  $S$  to 51.9%. As already reported,<sup>8</sup> this result demonstrates that possible drawbacks of up-to-date gas sensors, such as aging effects and fabrication reliability, can be effectively addressed.

By further comparison of experimental data in Figure 3 and Figure S1, which refer to parallel-plate and comb-type source/drain terminal configurations, respectively, it is apparent that high reliability over time (up to 48 h) (Figure 3a,b and Figure S1a,b) and high linearity of the calibration curve (Figure 3c and Figure S1c) are achieved for all the tested sensors, independently of both source/drain configuration and  $W/L$  ratio. As expected and coherently with the channel width-to-length ratio ( $W/L$ ) of the fabricated JFET devices, the different sensors feature different  $I_{DS}$  current values under exposure to both air and  $\text{NO}_2$  (Figure 3a,b and Figure S1a,b). For instance,  $I_{DS}$  values are in the range of 20  $\mu\text{A}$  (absolute value) for sensors with  $W = 300\text{ }\mu\text{m}$ , up to 1.8 mA (absolute value) for sensor with  $W = 7500\text{ }\mu\text{m}$ , in air at  $V_{GS} = 0\text{ V}$ . A comparison of time-resolved response curves of four cSiAuJFETs integrated on the same silicon die with different source/drain terminal configurations and different  $W/L$  ratios is reported in Figure S2a.

It is worth noting that, sensors with parallel-plate drain/source configuration (smaller  $W/L$  ratio) show higher relative current variation and, in turn, sensitivity value (Figure 3c), with respect to those with comb-type configuration (larger  $W/L$  ratio) (Figure S1c in the Supporting Information). A comparison between calibration curves ( $\Delta I_R$  versus  $\text{NO}_2$  concentration) of four cSiAuJFETs integrated on the same silicon die with different source/drain terminal configurations, at  $V_{GS} = 1.5\text{ V}$ , is provided in Figure S2b. Moreover, a quadratic dependence of the sensitivity value on the gate voltage  $V_{GS}$  value occurs for parallel-plate cSiAuJFETs independently of channel widths, whereas the dependence is linear for comb-type cSiAuJFETs, which means that electrical tuning of the sensitivity is more effective for the former with respect to the latter. We argue that such a difference between parallel-plate and comb-type sensors is mainly related to slight variations in either thickness or surface area of the cSiAuN layer induced by the different device patterns (e.g., because of corner effects) on the MAE outcomes.

## 5. CONCLUSIONS

In this work, metal-assisted etching (MAE) is successfully demonstrated for the first time as a powerful approach for the integration of composite silicon/metal nanostructured materials, specifically composite porous silicon/gold nanostructures (cSiAuNs), into JFET transistors, for the realization of a novel class of metal-doped silicon-based chemi-transistor gas sensors, namely cSiAuJFET. The cSiAuJFET sensors operate at room temperature and show fast and reliable response to  $\text{NO}_2$  in the range 100–500 ppb without significant aging effects up to 48 h of continuous operation, in terms of baseline drift, response times, and sensitivity value. Moreover, real-time and effective tuning of the sensitivity of cSiAuJFET sensors by controlling the electrical bias  $V_{GS}$  of the transistor gate-terminal is demonstrated and no significant effects of the different  $V_{GS}$  voltage values on response times are seen.

Long-term measurements aimed at addressing possible performance degradation of cSiAuJFET sensors beyond 48 h of operation, for example, because of aging (oxidation) of the porous silicon matrix, and interference measurements aimed at establishing the degree of selectivity of cSiAuJFET sensors, for example, toward other species (relative humidity) present in the environment, will be subject of future work.

The proposed approach for the fabrication of metal-doped silicon-based chemi-transistor sensors exploiting composite porous silicon/gold nanostructures prepared by metal-assisted etching also envisages the possibility of tuning the sensor performance by selecting ad-hoc metal catalysts (e.g., Ag, Pt, etc.), thus paving a way toward the CMOS integration of chemi-transistor sensors with improved selectivity, lifetime, and reliability toward specific analytes, as well as improved environmental sustainability. As a consequence, a further outcome is the simultaneous integration on the same silicon chip of chemi-transistors with different metal dopants, that is exploiting different nanostructured silicon/metal composites, and, in turn, with different sensing features. This would lead to the development of an array of miniaturized sensors with electronically addressable metal-doped silicon nanostructures for E-nose applications.

Applications for these small-size, low-power electronic sensor arrays are in detection and identification of toxic/explosive gases for personal safety and air pollution monitoring, but also in the chemical and biological sensing field.

## 6. EXPERIMENTAL SECTION

**Preparation of Composite Porous Silicon/Gold Nanostructures.** Composite porous silicon/gold nanostructures are produced both on p<sup>+</sup>-type (resistivity of 0.04  $\Omega$  cm) and on p-type (resistivity of 2.5–4  $\Omega$  cm) CZ-grown, (100)-oriented, silicon substrates by using the MAE of silicon as given in literature.<sup>25,27</sup> The Si substrates are first cleaned to remove organic grease by soaking in acetone (99%, Sigma-Aldrich) and ethanol (99.8%, Fluka Analytical) in ultrasonic bath at room temperature for 10 and 5 min, respectively, then rinsed in deionized water two times and blown using dry nitrogen gas. Afterward, the native silicon dioxide is removed by wet etching in a HF (48%, Sigma-Aldrich):ethanol (99.8%, Fluka Analytical) solution (1:1 by vol). Subsequently, Au nanoparticles from 2 mm  $\times$  2 mm pellets of 99.95% purity gold (Testbourne Ltd.) are deposited by electron beam-assisted thermal evaporation (homemade assembled using Edwards parts) at room temperature and residual pressure of  $1 \times 10^{-5}$  mbar on top of the cleaned Si substrates. In our experiments different nominal thicknesses of gold, namely 0.7, 1.5, and 3 nm, are deposited at rate of about 3 nm/min. The Si samples coated with gold NPs on top are immersed in an aqueous solution of hydrofluoric acid (HF, 48%, Sigma-Aldrich) and hydrogen peroxide (H<sub>2</sub>O<sub>2</sub>, 30%, Sigma-Aldrich) for different times (30, 60, 90 s) in order to produce the composite porous silicon/gold nanostructures. Each experiment is repeated three times in order to evaluate the average and standard deviation values. The concentrations of HF and H<sub>2</sub>O<sub>2</sub> (1:1 by vol.) in the etching solution are chosen according to the literature on this subject so as to enhance reproducibility and uniformity of the resulting nanostructured material.<sup>40</sup> A polytetrafluoroethylene (PTFE) cell that allows the front side of the gold-coated samples to be put in contact with the etching solution is used as experimental setup to perform the MAE. When the etching process is over, the samples are rinsed with ethanol (99.8%, Fluka Analytical), then with pentane (99%, Sigma-Aldrich), and eventually dried under nitrogen gas flow for 20 min.

**Integration of Porous Silicon/Gold Nanostructures into JFET Devices.** The cSiAuJFET is fabricated on pn-type silicon wafers (nominal resistivity of p-type and n-type silicon of 0.04  $\Omega$  cm and 2–4  $\Omega$  cm, respectively). The metallurgical junction between p- and n-type silicon is located at 2.3  $\mu$ m from the top. A thermal evaporation of 500 nm thick aluminum film is performed on both p-type silicon (front-side surface) and n-type silicon (back-side surface) under a residual pressure of  $1 \times 10^{-5}$  mbar. Source and drain contacts (both parallel-plate and comb-type in shape) are defined (1st mask) on the aluminum film deposited on top of the p-type silicon (front-side surface) by using standard UV photolithography steps: (i) positive photoresist (Microposit S1818 G2, Rhom and Haas) spinning at 5000 rpm for 30 s and subsequent prebaking at 115  $^{\circ}$ C for 75 s on hot plate; (ii) UV exposure of the photoresist by using a contact lithography system (MJB3 Karl-Suss mask aligner); (iii) photoresist development using a Microposit 351 Developer (Rhom and Haas):H<sub>2</sub>O (deionized) 1:5 by volume solution and subsequent postbaking at 115  $^{\circ}$ C for 75 s on hot plate. Chemical etching of aluminum through the patterned photoresist is performed at room temperature for 5 min in a solution of H<sub>3</sub>PO<sub>4</sub> (85%):HNO<sub>3</sub> (65%):CH<sub>3</sub>COOH (99.5%):H<sub>2</sub>O = 16:1:1:2 (by vol). The sample is then rinsed in acetone (99%, Sigma-Aldrich) and ethanol (99.8%, Fluka Analytical) for 15 and 5 min, respectively, in order to fully dissolve the residual photoresist and clean the sample surface. Source and drain aluminum contacts are then protected using a photoresist layer patterned by UV photolithography (2nd mask) using a magnified replica of the first mask that allows the aluminum contacts to be overlapped by photoresist for a width of 50  $\mu$ m. Electron beam-assisted thermal evaporation of a 1.5 nm thick gold (pellet, 99.95% purity, Testbourne Ltd.) film is carried out on the front-side surface of the samples, thus enabling deposition of Au nanoparticles on the photoresist-free p-type silicon surface between drain and source contacts.

The selective gold-assisted etching of part of the p-type silicon between drain and source contacts is performed with a HF (48%, Sigma-Aldrich):H<sub>2</sub>O<sub>2</sub> (30%, Sigma-Aldrich) = 1:1 (by vol) solution for 90 s, so as to integrate the composite porous silicon/gold nanostructured layer on top of the JFET p-channel. A rinse of the

sample in acetone (99%, Sigma-Aldrich) and then in ethanol (99.8%, Fluka Analytical) for 15 and 5 min, respectively, is performed to completely remove the photoresist mask covered with gold NPs and clean the sample surface, then the sample is dried under nitrogen gas flow for 20 min.

**SEM and XPS Analysis.** The as-synthesized samples were studied using a scanning electron microscope (SEM) JEOL JSM-6390 at an acceleration voltage of 3 kV.

XPS measurements are performed using an Axis ULTRA DLD Spectrometer (Kratos Analytical, UK) with a monochromatic Al K $\alpha$  source operating at 225 W (15 kV, 15 mA). For each sample a wide-scan spectrum (WS) is acquired in the binding energy range 0–1200 eV with a pass energy of 160 and 1 eV step, while high-resolution regions are acquired with a pass energy of 20 and 0.1 eV step. In both cases, the area of analysis is about 700  $\times$  300  $\mu$ m<sup>2</sup>. The base pressure in the instrument is  $1 \times 10^{-9}$  mbar. Data analysis and peak fitting is performed by CasaXPS software. Surface charging is corrected considering adventitious C 1s (BE = 285 eV).

**Electrical Characterization of the Chemi-Transistors.** The sensor characterization under calibrated concentrations of NO<sub>2</sub> in air is carried out using the flow-through technique. The die integrating several cSiAuJFET devices is mounted onto a TO-8 package and placed in a stainless steel test chamber with volume of about 10 cm<sup>3</sup> and temperature controlled with accuracy of  $\pm 0.5$   $^{\circ}$ C. For all the experiments, the gas flow-rate in the test chamber is maintained at 200 standard cubic centimeter per minute (sccm), synthetic air (5.0 compressed dry air, Rivoira) is used as carrier gas, NO<sub>2</sub> (1000 ppb in dry air, Rivoira) as target gas, relative humidity is set to zero, and temperature is set to 25  $^{\circ}$ C. Two digital mass flow controllers (1179B, MKS Instruments) and a digital driving/readout system (PR4000, MKS Instruments) are used to produce synthetic air/NO<sub>2</sub> mixtures with NO<sub>2</sub> concentrations of 0–100–300–500 ppb.

Time-resolved curves (current versus time) of the cSiAuJFETs are measured by biasing the sensors in the saturation region. A Picoammeter/Voltage source (6487, Keithley Instruments), which is used to contemporarily set the voltage  $V_{DS} = -2$  V and measure the current  $I_{DS}$  between the drain and source terminals over time. A Source-Meter unit (2400, Keithley Instruments) is used to set the voltage  $V_{GS}$  at different values, namely 0, 0.7, 1.5, and 2.5 V, and simultaneously measure the current  $I_G$  between gate (electrical) and source terminals. The cSiAuJFETs are exposed to synthetic air in the test chamber for 60 min prior to exposure to NO<sub>2</sub> in order to settle the output response of the sensor to a stable current value (warm up period). Afterward, the devices are exposed to NO<sub>2</sub> for 30 min (adsorbing phase) and then to synthetic air for 60 min (desorbing phase), repeating the method on the entire NO<sub>2</sub> concentration window (100–300–500 ppb), whereas the voltage gate is tuned to a new value at the end of each adsorbing phase of 500 ppb.

The measure system is PC-controlled using a LabView interface designed to guarantee the correct timing among of all the different equipment. This comprehends driving the flow controller for setting the right NO<sub>2</sub> concentration and driving the electrical measurement units for recording the current of each cSiAuJFET on the chip.

## ■ ASSOCIATED CONTENT

### Supporting Information

Characterization and performance of comb-type cSiAuJFET sensors and comparison of four cSiAuJFETs integrated on the same silicon die. This material is available free of charge via the Internet at <http://pubs.acs.org/>

## ■ AUTHOR INFORMATION

### Corresponding Author

\*E-mail: [g.barillaro@iet.unipi.it](mailto:g.barillaro@iet.unipi.it).

### Notes

The authors declare no competing financial interest.



## REFERENCES

- (1) Europe to Exceed Air Pollutant Emission Limits – NO<sub>x</sub> in Particular; European Environment Agency: Copenhagen, Denmark, 2010; <http://www.eea.europa.eu/highlights/europe-to-exceed-air-pollutant> (accessed October 2014).
- (2) Documentation for Immediately Dangerous To Life or Health Concentrations (IDLHs); The National Institute for Occupational Safety and Health (NIOSH), Centers for Disease Control and Prevention: Atlanta, GA, 1994; <http://www.cdc.gov/niosh/idlh/default.html> (accessed October 2014).
- (3) Afzal, A.; Cioffi, N.; Sabbatini, L.; Torsi, L. NO<sub>x</sub> Sensors Based on Semiconducting Metal Oxide Nanostructures: Progress and Perspectives. *Sens. Actuators, B* **2012**, 171–172, 25–42.
- (4) Torsi, L.; Dodabalapur, A. Organic Thin-Film Transistors as Plastic Analytical Sensors. *Anal. Chem.* **2005**, 77, 380A–387A.
- (5) Knopfmacher, O.; Hammock, M. L.; Appleton, A. L.; Schwartz, G.; Mei, J.; Lei, T.; Pei, J.; Bao, Z. Highly Stable Organic Polymer Field-Effect Transistor Sensor for Selective Detection in the Marine Environment. *Nat. Commun.* **2014**, 5, 2954.
- (6) Lee, K.; Ju, B.-K. Carbon-Nanotube-Based Flexible Devices Using a Mechanical Transfer Method. *Phys. Status Solidi A* **2012**, 209, 2082–2086.
- (7) Guo, Y.; Wu, B.; Liu, H.; Ma, Y.; Yang, Y.; Zheng, J.; Yu, G.; Liu, Y. Electrical Assembly and Reduction of Graphene Oxide in a Single Solution Step for Use in Flexible Sensors. *Adv. Mater.* **2011**, 23, 4626–4630.
- (8) Lazzarini, G. M.; Strambini, L. M.; Barillaro, G. Addressing Reliability and Degradation of Chemitranstors Sensors By Electrical Tuning of the Sensitivity. *Sci. Rep.* **2013**, 3, 1161.
- (9) Zhang, D.; Liu, Z.; Li, T.; Tang, C.; Liu, X.; Han, S.; Lei, B.; Zhou, C. Detection of NO<sub>2</sub> Down to ppb Levels Using Individual and Multiple In<sub>2</sub>O<sub>3</sub> Nanowire Devices. *Nano Lett.* **2004**, 4, 1919–1924.
- (10) Das, A.; Dost, R.; Richardson, T.; Grell, M.; Morrison, J. J.; Turner, M. L. A Nitrogen Dioxide Sensor Based on an Organic Transistor Constructed from Amorphous Semiconducting Polymers. *Adv. Mater.* **2007**, 19, 4018–4023.
- (11) McAlpine, M. C.; A. H.; Wang, D.; Heath, J. R. Highly Ordered Nanowire Arrays on Plastic Substrates for Ultrasensitive Flexible Chemical Sensors. *Nat. Mater.* **2007**, 6, 379–384.
- (12) Paska, Y.; Stelzner, T.; Christiansen, S.; Haick, H. Enhanced Sensing of Nonpolar Volatile Organic Compounds by Silicon Nanowire Field Effect Transistors. *ACS Nano* **2011**, 5, 5620–5626.
- (13) Santoro, G.; Yu, S.; Schwartzkopf, M.; Zhang, P.; Vayalil, S. K.; Risch, J. F. H.; Rübhausen, M. A.; Hernández, M.; Domingo, C.; V. R. S. Silver Substrates for Surface Enhanced Raman Scattering: Correlation Between Nanostructure and Raman Scattering Enhancement. *Appl. Phys. Lett.* **2014**, 104, 243107.
- (14) Zou, X.; Wang, J.; Liu, X.; Wang, C.; Jiang, Y.; Wang, Y.; Xiao, X.; Ho, J. C.; Li, J.; Jiang, C.; Fang, Y.; Liu, W.; Liao, L. Rational Design of Sub-Parts per Million Specific Gas Sensors Array Based on Metal Nanoparticles Decorated Nanowire Enhancement-Mode Transistors. *Nano Lett.* **2013**, 13, 3287–3292.
- (15) Kauffman, D. R.; Star, A. Chemically Induced Potential Barriers at the Carbon Nanotube–Metal Nanoparticle Interface. *Nano Lett.* **2007**, 7, 1863–1868.
- (16) Han, N.; Wang, F.; Hou, J. J.; Yip, S. P.; Lin, H.; Xiu, F.; Fang, M.; Yang, Z.; Shi, X.; Dong, G.; Hung, T. F.; Ho, J. C. Tunable Electronic Transport Properties of Metal-Cluster-Decorated III-V Nanowire Transistors. *Adv. Mater.* **2013**, 25, 4445–4451.
- (17) Ieva, E.; Bulchholt, K.; Colaianni, L.; Cioffi, N.; Sabbatini, L.; Capitani, G. C.; Lloyd Spetz, A.; Kall, P. O.; Torsi, L. Au Nanoparticles as Gate Material for NO<sub>x</sub> Field Effect Capacitive Sensors. *Sens. Lett.* **2008**, 6, 577–584.
- (18) Cioffi, N.; Colaianni, L.; Ieva, E.; Pilolli, R.; Ditaranto, N.; Angione, M. D.; Cotrone, S.; Buchholt, K.; Lloyd Spetz, A.; Sabbatini, L.; Torsi, L. Electrosynthesis and Characterization of Gold Nanoparticles for Electronic Capacitance Sensing of Pollutants. *Electrochim. Acta* **2011**, 56, 3713–3720.
- (19) Ahn, J.-H.; Yun, J.; Choi, Y.-K.; Park, I. Palladium Nanoparticle Decorated Silicon Nanowire Field-Effect Transistor With Side-Gates for Hydrogen Gas Detection. *Appl. Phys. Lett.* **2014**, 104, 013508.
- (20) Peng, K.-Q.; Yan, Y.-J.; Gao, S.-P.; Zhu, J. Synthesis of Large-Area Silicon Nanowire Arrays via Self-Assembling Nanoelectrochemistry. *Adv. Mater.* **2002**, 14, 1164–1167.
- (21) Boarino, L.; Imbraguglio, D.; Enrico, E.; De Leo, N.; Celegato, F.; Tiberto, P.; Pugno, N.; Amato, G. Fabrication of Ordered Silicon Nanopillars and Nanowires By Self-Assembly and Metal-Assisted Etching. *Phys. Status Solidi A* **2011**, 208, 1412–1416.
- (22) Peng, K. Q.; Wang, X.; Wu, X. L.; Lee, S. T. Platinum Nanoparticle Decorated Silicon Nanowires for Efficient Solar Energy Conversion. *Nano Lett.* **2009**, 9, 3704–3709.
- (23) Garnett, E. C.; Yang, P. Silicon Nanowire Radial p-n Junction Solar Cells. *J. Am. Chem. Soc.* **2008**, 130, 9224–9225.
- (24) Peng, K.-Q.; Wang, X.; Lee, S.-T. Gas Sensing Properties of Single Crystalline Porous Silicon Nanowires. *Appl. Phys. Lett.* **2009**, 95, 243112.
- (25) Li, X. Metal Assisted Chemical Etching for High Aspect Ratio Nanostructures: a Review of Characteristics and Applications in Photovoltaics. *Curr. Opin. Solid State Mater. Sci.* **2012**, 16, 71–81.
- (26) Peng, K.; Wu, Y.; Fang, H.; Zhong, X.; Xu, Y.; Zhu, J. Uniform, Axial-Orientation Alignment of One-Dimensional Single-Crystal Silicon Nanostructure Arrays. *Angew. Chem., Int. Ed.* **2005**, 44, 2737–2742.
- (27) Scheeler, S. P.; Ullrich, S.; Kudera, S.; Pacholski, C. Fabrication of Porous Silicon By Metal-Assisted Etching Using Highly Ordered Gold Nanoparticle Arrays. *Nanoscale Res. Lett.* **2012**, 7, 450.
- (28) Lehmann, H. W.; Frick, K. Optimizing Deposition Parameters of Electron Beam Evaporated TiO<sub>2</sub> Films. *Appl. Opt.* **1988**, 27, 4920–4924.
- (29) Zhang, Y.; Franklin, N. W.; Chen, R. J.; Dai, H. Metal Coating on Suspended Carbon Nanotubes and its Implication to Metal-Tube Interaction. *Chem. Phys. Lett.* **2000**, 331, 35–41.
- (30) Dawood, M. K.; Tripathy, S.; Dolmanan, S. B.; Ng, T. H.; Tan, H.; Lam, J. Influence of Catalytic Gold and Silver Metal Nanoparticles on Structural, Optical, and Vibrational Properties of Silicon Nanowires Synthesized by Metal-Assisted Chemical Etching. *J. Appl. Phys.* **2012**, 112, 073509.
- (31) Gaspar, D. P. A. C.; Mateus, T.; Leitao, J. P.; Soares, J.; Falcao, B. P.; Araujo, A.; Vicente, A.; Filonovich, S. A.; Aguas, H.; Martins, R.; Ferreira, I. Influence Of The Layer Thickness In Plasmonic Gold Nanoparticles Produced By Thermal Evaporation. *Sci. Rep.* **2013**, 3, 1469.
- (32) Lehmann, V. *Electrochemistry of Silicon: Instrumentation, Science, Materials and Applications*; Wiley–VCH: Weinheim, Germany, 2002.
- (33) Huang, Z.; Geyer, N.; Werner, P.; de Boor, J.; Gosele, U. Metal-Assisted Chemical Etching of Silicon: a Review. *Adv. Mater.* **2011**, 23, 285–308.
- (34) Chern, W.; Hsu, K.; Chun, I. S.; Azeredo, B. P.; Ahmed, N.; Kim, K. H.; Zuo, J. M.; Fang, N.; Ferreira, P.; Li, X. Nonlithographic Patterning and Metal-Assisted Chemical Etching for Manufacturing of Tunable Light-Emitting Silicon Nanowire Arrays. *Nano Lett.* **2010**, 10, 1582–1588.
- (35) Tsakalakos, L.; Balch, J.; Fronheiser, J.; Korevaar, B. A.; Sulima, O.; Rand, J. Silicon Nanowire Solar Cells. *Appl. Phys. Lett.* **2007**, 91, 233117.
- (36) Peng, K. Q.; Hu, J. J.; Yan, Y. J.; Wu, Y.; Fang, H.; Xu, Y.; Lee, S. T.; Zhu, J. Fabrication of Single-Crystalline Silicon Nanowires by Scratching a Silicon Surface with Catalytic Metal Particles. *Adv. Funct. Mater.* **2006**, 16, 387–394.
- (37) Cruz, S.; Hönig-d'Orville, A.; Müller, J. Fabrication and Optimization of Porous Silicon Substrates for Diffusion Membrane Applications. *J. Electrochem. Soc.* **2005**, 152, C418–C424.
- (38) Peng, K.; Lu, A.; Zhang, R.; Lee, S.-T. Motility of Metal Nanoparticles in Silicon and Induced Anisotropic Silicon Etching. *Adv. Funct. Mater.* **2008**, 18, 3026–3035.

- (39) Laminack, W. I.; Gole, J. L. Light Enhanced Electron Transduction and Amplified Sensing at a Nanostructure Modified Semiconductor Interface. *Adv. Funct. Mater.* **2013**, *23*, 5916–5924.
- (40) Oh, Y.; Choi, C.; Hong, D.; Kong, S. D.; Jin, S. Magnetically Guided Nano-Micro Shaping and Slicing of Silicon. *Nano Lett.* **2012**, *12*, 2045–2050.
- (41) Patolsky, F.; Zheng, G.; Lieber, C. M. Fabrication of Silicon Nanowire Devices for Ultrasensitive, Label-Free, Real-Time Detection of Biological and Chemical Species. *Nat. Protoc.* **2006**, *1*, 1711–1724.
- (42) Zhao, L.; Siu, A. C.-L.; Petrus, J. A.; He, Z.; Leung, K. T. Interfacial Bonding of Gold Nanoparticles on a H-terminated Si(100) Substrate Obtained by Electro- and Electroless Deposition. *J. Am. Chem. Soc.* **2007**, *129*, 5730–5734.
- (43) Fabre, B.; Hennous, L.; Ababou-Girard, S.; Meriadec, C. Electroless Patterned Assembly of Metal Nanoparticles on Hydrogen-Terminated Silicon Surfaces for Applications in Photoelectrocatalysis. *ACS Appl. Mater. Interfaces* **2013**, *5*, 338–343.
- (44) Sundaravel, B. S. K.; Kuri, G.; Satyam, P. V.; Dev, B. N.; Bera, S.; Narasimhan, S. V.; Chakraborty, P.; Caccavale, F. XPS And SIMS Analysis of Gold Silicide Grown on a Bromine Passivated Si(111) Substrate. *Appl. Surf. Sci.* **1999**, *137*, 103–112.
- (45) Sayed, S. Y.; Wang, F.; Malac, M.; Meldrum, A.; Egerton, R. F.; Buriak, J. M. Heteroepitaxial Growth of Gold Nanostructures on Silicon by Galvanic Displacement. *ACS Nano* **2009**, *3*, 2809–2817.
- (46) Forleo, A.; Francioso, L.; Capone, S.; Siciliano, P.; Lommens, P.; Hens, Z. Synthesis and Gas Sensing Properties of ZnO Quantum Dots. *Sens. Actuators, B* **2010**, *146*, 111–115.
- (47) Boarino, L.; Geobaldo, F.; Borini, S.; Rossi, A.; Rivolo, P.; Rocchia, M.; Garrone, E.; Amato, G. Local Environment of Boron Impurities in Porous Silicon and Their Interaction with NO<sub>2</sub> Molecules. *Phys. Rev. B* **2001**, *64*, 205308.
- (48) Timoshenko, V.; Dittrich, T.; Lysenko, V.; Lisachenko, M.; Koch, F. Free Charge Carriers in Mesoporous Silicon. *Phys. Rev. B* **2001**, *64*, 085314.
- (49) Barillaro, G.; Lazzerini, G. M.; Strambini, L. M. Modeling of Porous Silicon Junction Field Effect Transistor Gas Sensors: Insight Into NO<sub>2</sub> Interaction. *Appl. Phys. Lett.* **2010**, *96*, 162105.
- (50) Borini, S.; Boarino, L.; Amato, G. Slow Conductivity Relaxation and Simple Aging in Nanostructured Mesoporous Silicon at Room Temperature. *Phys. Rev. B* **2007**, *75*, 165205.
- (51) Zhang, Y.; Kolmakov, A.; Chretien, S.; Metiu, H.; Moskovits, M. Control of Catalytic Reactions at the Surface of a Metal Oxide Nanowire by Manipulating Electron Density Inside It. *Nano Lett.* **2004**, *4*, 403–407.
- (52) Mubeen, S.; Moskovits, M. Gate-Tunable Surface Processes on a Single-Nanowire Field-Effect Transistor. *Adv. Mater.* **2011**, *23*, 2306–2312.